https://dx.doi.org/10.1016/j.mechmat.2023.104823

Numerical modeling of the mechanical response of asphalt concrete in tension and compression

Zhifei Tan[a,b], Zhen Leng[a,b*], Denis Jelagin[c], Peng Cao[d], Jiwang Jiang[a,b,e], Prabin Kumar Ashish[a,f], Fuliao Zou[a,b]

[a] Department of Civil and Environmental Engineering, The Hong Kong Polytechnic University, Hong Kong, China

[b] Research Center for Resources Engineering Towards Carbon Neutrality, The Hong Kong Polytechnic University, Hong Kong, China

[c] Department of Civil and Architectural Engineering, KTH Royal Institute of Technology, Brinellvägen 23, 10044, Stockholm, Sweden

[d] College of Architecture and Civil Engineering, Beijing University of Technology, Beijing, China

[e] School of Transportation, Southeast University, Nanjing 210000, Jiangsu, China

[f] Department of Civil Engineering, Indian Institute of Technology Kanpur, India

Corresponding Authors*

Zhen Leng, Email: zhen.leng@polyu.edu.hk

Abstract

Asphalt concrete (AC) shows significant tension-compression (TC) asymmetry, i.e., different properties in tension and compression (T&C). This asymmetry may profoundly affect AC's performance and deterioration in the field, but limited studies have been performed to quantify this behavior. This study aims to quantitively characterize the global and local mechanical responses of AC in T&C through numerical modeling. To this end, three AC mixtures: the gap-graded SMA10, dense-graded AC20, and open-graded mixtures PA13, were evaluated experimentally and numerically. Digital image processing was used to generate image-based AC models with contact regions (CR), and dynamic simulations were conducted using the steady-state dynamics (SSD) approach. The results indicated that the measured and predicted master curves for AC in T&C qualitatively agree and demonstrate significant asymmetry, with higher moduli but lower phase angles in compression compared to tension. Among the mixtures, PA13 exhibited the most pronounced asymmetry, followed by SMA10 and AC20. Statistical analyses of local stress and strain found that the stress and strain in different phases show significant variations, with more pronounced disparities observed at lower frequencies. Notably, at 10^{-6} Hz for PA13 in compression, the stress within the aggregate phase exceeded that of the matrix phase by over 250 times, while the strain within the matrix phase surpassed the aggregate phase by more than 600 times. To enhance pavement durability, it is recommended to consider AC's TC asymmetry in pavement design.

Keywords: Tension-compression asymmetry, Numerical modeling, Internal mechanical properties, Aggregate contact, Finite element analysis

1. Introduction

Asphalt concrete (AC) exhibits significant tension-compression (TC) asymmetry, a phenomenon widely observed in previous studies (Katicha et al., 2010; Khanal and Mamlouk, 1995; Monismith and Secor, 1962; Nguyen et al., 2016; Pister and Westmann, 1962). TC asymmetry refers to the load-direction dependency of AC's response. In compression, AC generally displays much higher moduli compared to tension (Dai et al., 2021; Keshavarzi and Kim, 2016; Lv et al., 2018; Lytton et al., 2018; Nguyen et al., 2016). Previous research has shown that the compressive moduli of AC are 1.5 to 2 times higher than the tensile moduli (Zhang et al., 2012), while the compressive strength of AC has been reported to be ten times higher than its tensile strength (Hargett and Johnson, 1961). It was also found that AC's TC asymmetry is temperature- and time-dependent (Khanal and Mamlouk, 1995; Lytton et al., 2018), with higher temperatures or lower loading rates making this phenomenon more remarkable (Cheng et al., 2021). Considering the heterogeneity of AC (Song et al., 2023, 2021), many studies attributed the TC asymmetry behavior of AC to the packing structure of aggregates (Levenberg, 2015; Lytton et al., 1993). The phenomenological explanation is that AC's aggregate structure is pulled apart in tension whereas pushed closer in compression, leading to more contribution from aggregates to the AC mechanical response in compression (Cheng et al., 2021; Jiang et al., 2021; Levenberg, 2015; Lytton et al., 1993). However, this speculation does not fully elucidate the underlying mechanisms. A recent study demonstrated that the aggregate contact effect is the primary factor behind AC's TC asymmetry (Tan et al., 2023). The results indicated that aggregate contacts lead to microscale TC asymmetry in the contact region (CR), which further manifests as macroscale asymmetric performance of AC (Tan et al., 2023). The modeling method proposed in this study offers a feasible approach to characterize the internal mechanical properties underlying this TC asymmetric behavior.

With the advancement of computational methods, it has become feasible to simulate the internal mechanical behavior of AC using micromechanical models (Cai et al., 2020; Cao et al., 2017; Du et al., 2021; Jiang et al., 2022; Liu et al., 2018). In numerical micromechanical modeling, AC is typically treated as a composite consisting of three phases: aggregate, matrix, and air void (Cao et al., 2019; Song et al., 2023; Sun et al., 2021). Digital image processing (DIP) techniques are commonly

employed to generate realistic microstructures of AC (Liu et al., 2018; Onifade et al., 2016; Tan et al., 2022). Due to their efficiency, 2D microstructural models of AC are widely utilized (Cai et al., 2023; Kollmann et al., 2019; Ling et al., 2017). However, in recent years, more complex 3D micromechanical models have been developed (Jin et al., 2021; Liu et al., 2017; Lu et al., 2019). Although these 3D models come with increased computational costs, they offer improved realism and can significantly enhance modeling accuracy. By employing these micromechanical models, it becomes possible to predict the internal mechanical response of AC under external loads, such as dynamic and traffic loads (Gong et al., 2023; Sun et al., 2022; Wollny et al., 2020). However, a major limitation of existing micromechanical models for AC is the lack of consideration for aggregate contact effects, which can greatly compromise prediction accuracy. Recent research pointed out that aggregate contacts also significantly affect AC's stability and rutting resistance (Jiang et al., 2017; Li et al., 2020; Ling and Bahia, 2018). Therefore, to achieve accurate predictions of AC's internal response, it is crucial to incorporate aggregate contact interactions into the modeling process.

In this study, the method proposed in (Tan et al., 2023, 2022) was adopted to introduce aggregate contacts into the micromechanical modeling of AC. One additional phase, CR, was incorporated into the developed microstructural model. CR, i.e., contact region or contact zone, represents the area of contact between neighboring aggregates (Tan et al., 2022). The surface distance threshold (SDT), which defines the maximum separation distance of aggregates considered to be in contact (Coenen et al., 2012; Kutay et al., 2010), was used to quantify the CR in AC. Therefore, the developed micromechanical model of AC consisted of four phases: aggregate, matrix, air void, and CR. Previous studies have validated that introducing the CR into the numerical model can significantly improve the prediction accuracy of AC in tension and compression (Tan et al., 2023, 2022). This study aims to evaluate and quantify the local and global mechanical response of AC in T&C. Due to the significant difference in the internal structures for different types of AC mixtures, the internal mechanical response of AC may vary dramatically. Therefore, three AC mixtures, including a gap-graded mixture (SMA10), a dense-graded mixture (AC20), and an open-graded mixture (PA13), are explored. In the modeling work, the micromechanical model of CR proposed in the previous study was adopted to predict the

viscoelastic properties for the CR in T&C (Tan et al., 2023). After that, the predicted viscoelastic properties were used as inputs for the CR phase in the micromechanical modeling of AC in T&C. By performing the dynamic simulation, the global viscoelastic properties and the local stress and strain response of the three AC mixtures can be predicted. It is worth noting that asphalt mastic and FAM are the matrix phases in the developed microstructural models of CR and AC, respectively. Therefore, frequency sweep tests were performed to measure their viscoelastic properties. The viscoelastic properties of the three AC mixtures in T&C were also measured for comparison with the numerically predicted values.

2. Theoretical Background

The mesostructural model of AC developed in this study comprises four phases: asphalt matrix (FAM), CR, aggregate, and air void. CR represents the composite of large filler particles, interfacial transition (ITZ) layers, and asphalt mastic at the microscale, as demonstrated in previous studies (Tan et al., 2023, 2022). Asphalt mastic, FAM, and CR (in tension or compression only) exhibit viscoelastic behavior under small strain levels. Therefore, their mechanical properties can be described by the following constitutive relationship:

$$\sigma(t) = \int_0^t E(t-\tau)\frac{d\varepsilon(\tau)}{d\tau}d\tau \quad (1)$$

where t represents time; τ is a time variable of integration; $E(t)$ is the relaxation modulus function in compression or tension. In the shear mode, the shear relaxation modulus function, $G(t)$, is used. Generally, the relaxation modulus function, $E(t)$, can be expressed in the form of Prony series as follows (Cho, 2016; Lakes, 1998; Tschoegl, 1989):

$$E(t) = E_0[1 - \sum_{i=1}^{n} g_i(1 - e^{-t/\tau_i})] \quad (2)$$

where E_0 is the instantaneous modulus; E_i and τ_i are the shear modulus and relaxation time for the i's Maxwell element; $g_i = \frac{E_i}{E_0}$ defines the weight of the i's Maxwell element; n is the number of Maxwell elements used to fit the equation. The relaxation modulus function can also be expressed in the frequency domain as follows (Ferry, 1980):

$$E'(\omega) = E_0[1 - \sum_{i=1}^{n} g_i] + E_0 \sum_{i=1}^{n} \frac{g_i {\tau_i}^2 \omega^2}{1 + {\tau_i}^2 \omega^2} \quad (3)$$

$$E^{"}(\omega) = E_0 \sum_{i=1}^{n} \frac{g_i \tau_i \omega}{1+\tau_i{}^2 \omega^2} \quad (4)$$

$$E^*(\omega) = E'(\omega) + iE''(\omega) \quad (5)$$

where E' and E'' denote the storage and loss moduli, respectively; ω is the angular frequency.

In this study, the measured complex modulus master curves of asphalt mastic and FAM, and the predicted master curves of CR in T&C were both converted to the format of Prony series for the numerical modeling.

3. Experimental Study

Three commonly used AC mixtures, including the gap-graded SMA10, dense-graded AC20, and open-graded PA13, were evaluated in this study. Figure 1 presents the aggregate gradations, while Table 1 provides the material properties for these mixtures. SMA10 and PA13 mixtures were prepared using a styrene-butadiene-styrene (SBS) modified binder with a Superpave performance grade of 76-16 (PG76-16), while AC20 utilized a virgin asphalt binder with a penetration grade of 60/70 (Pen60/70). The binder contents for SMA10, AC20, and PA13 were 6%, 5.2%, and 3.9%, respectively. Granitic aggregates were used in all mixtures. To characterize the viscoelastic properties of these mixtures at different length scales, namely asphalt mastic, FAM, and the AC mixture, master curves were constructed. Notably, to achieve a comprehensive frequency range, the Williams–Landel–Ferry (WLF) equation was utilized to shift the measured data to a reference temperature of 25 °C. The resulting data was then subjected to the modified Huet-Sayegh (MHS) model for further refinement (Zhang and Leng, 2017). Asphalt mastic, a mixture of asphalt binder and mineral filler (<0.075 mm), was measured to obtain the viscoelastic properties of CR (Tan et al., 2023). FAM represents the matrix phase in the developed micromechanical model of AC, consisting of asphalt mastic, mineral filler, and fine aggregates smaller than 2.36 mm (Leng et al., 2021; Zhang and Leng, 2017). Figure 2 illustrates the measurement setups at the three scales. The viscoelastic properties of asphalt mastic and FAM were measured using a dynamic shear rheometer (DSR) within the temperature range of -10 °C to 50 °C. The measured complex moduli were converted to master curves at a broader frequency range based on the time-temperature superposition principle, as shown in Figure 3. These master curves were then fitted using the Prony series model for numerical modeling. The viscoelastic properties of the AC

mixtures in compression and tension were measured using a universal testing machine (UTM), as depicted in Figures 2(c) and (d), respectively. The compressive dynamic test followed the guidelines of (AASHTO T 342, 2019). Three vertical linear variable differential transformers (LVDTs) were installed at a 120-degree interval on the cylindrical specimen. Dynamic tests were conducted with compressive sinusoidal loads at different frequencies (0.1, 0.5, 1.0, 5, 10, and 25 Hz) and temperatures (-10, 4.4, 21.1, 37.8, and 54 °C) to develop the master curves for the AC mixtures. For the tensile test, the top and bottom surfaces of the specimen were glued with steel plates, as shown in Figures 2(d). Due to the low modulus and instability of the tensile test at high temperatures, the measurement at 54 °C was not performed. Figure 4 presents the master curves for the AC mixtures in tension and compression. For simplicity, the '+' and '-' signs were used to represent tension and compression, respectively. The plot clearly shows significantly lower dynamic moduli and higher phase angles under tension mode compared to compression mode.

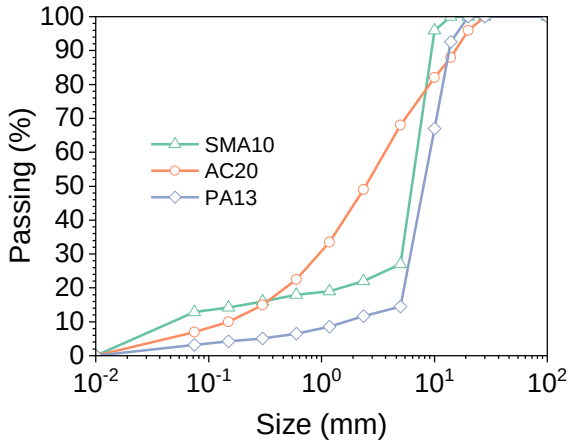

Figure 1 Gradation of the three AC mixtures

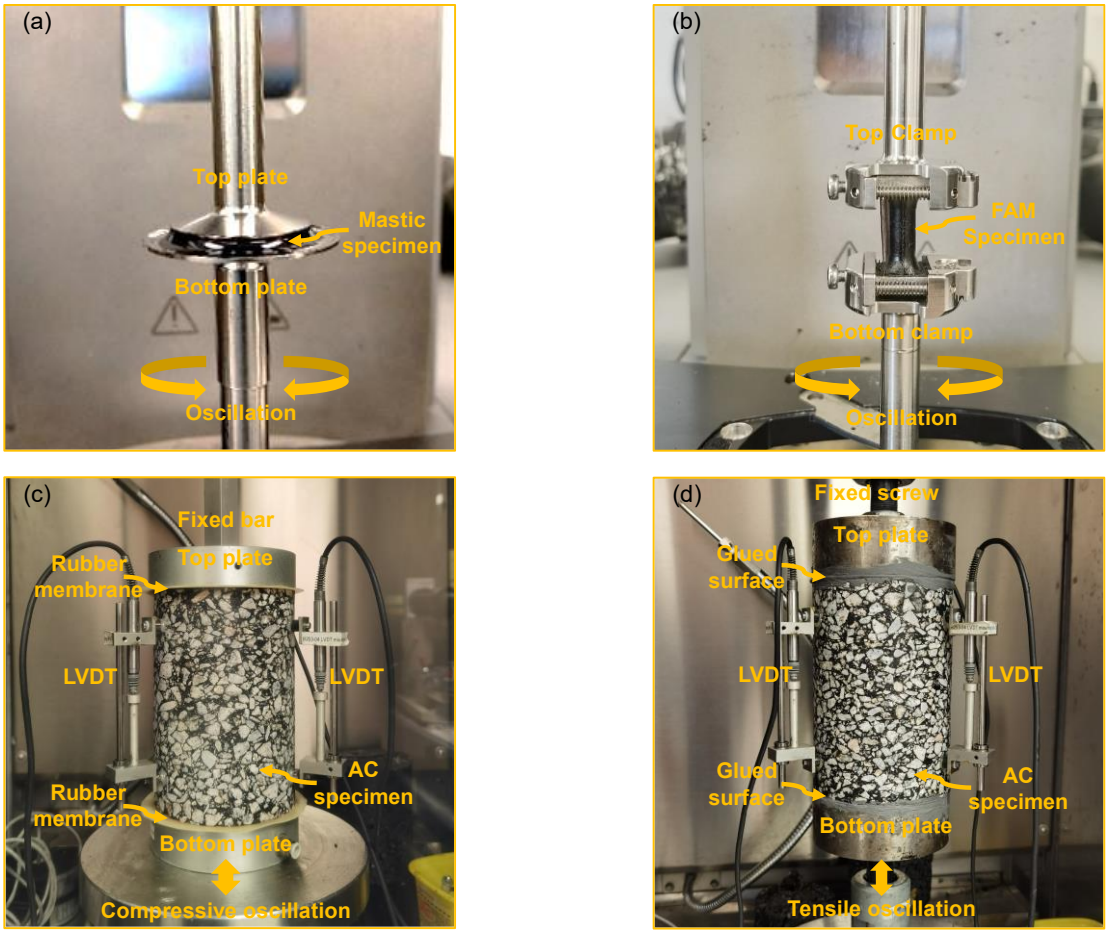

Figure 2 Test setups for: (a) asphalt mastic; (b) FAM; (c) AC in compression; and (d) AC in tension

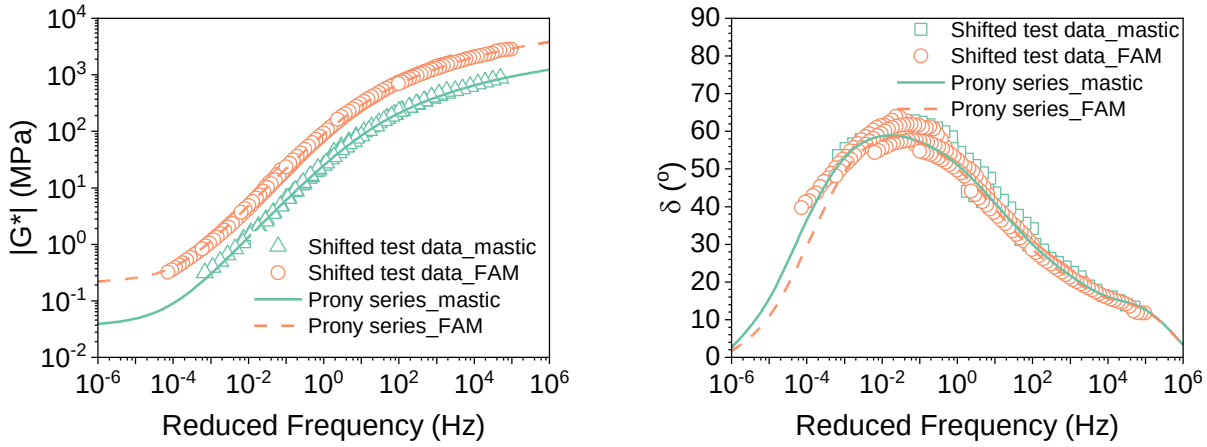

(a) Dynamic modulus (b) Phase angle

Figure 3 Measured master curves of asphalt mastic and FAM of SMA10 at 20 °C

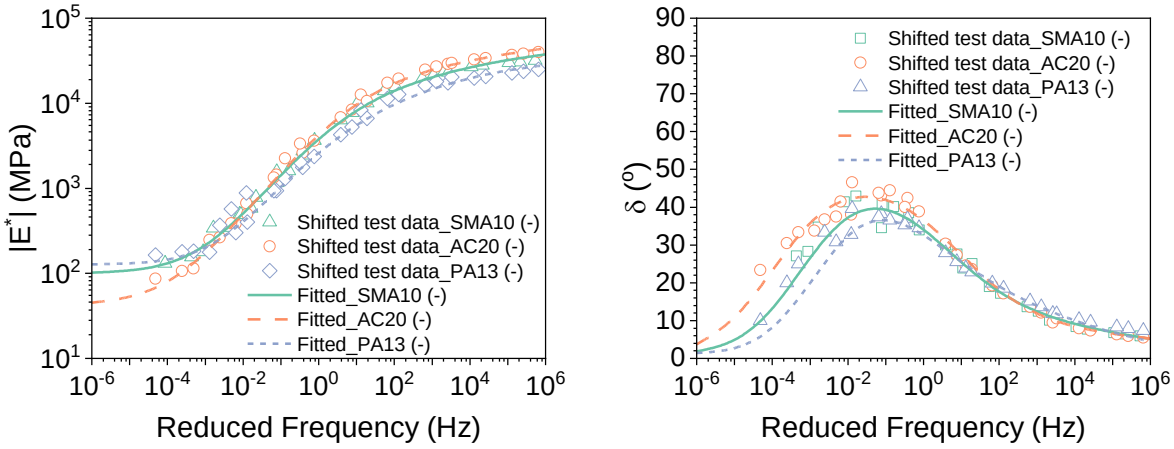

(a) Dynamic modulus in compression (b) Phase angle in compression

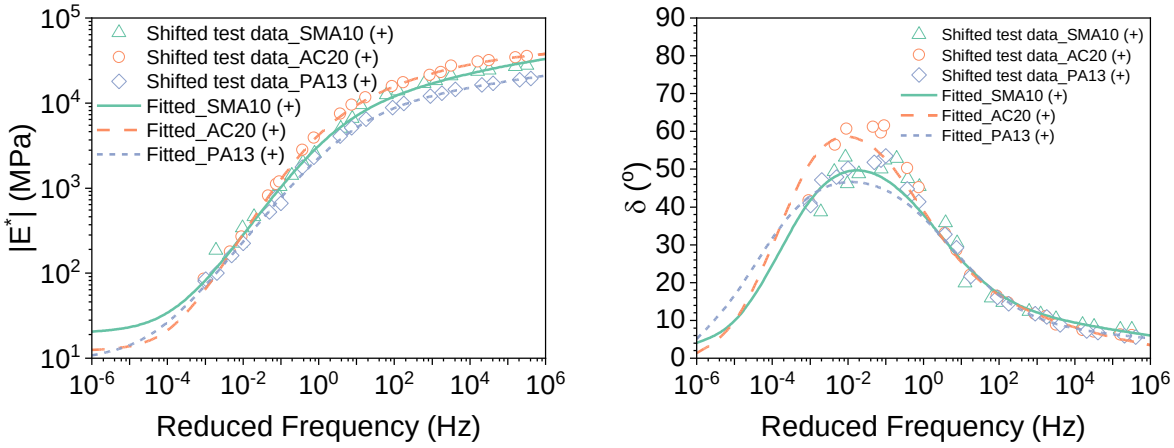

(c) Dynamic modulus in tension (d) Phase angle in tension

Figure 4 Measured master curves of the three AC mixtures in T&C at 20 °C

The internal structure of the AC mixtures was obtained using the X-ray CT scanning system of Phoenix v|tome|xs. The scanning was conducted at a resolution of 0.098 mm in all three directions. Figure 5 displays the images captured from the X-ray scanning of the specimens. The aggregates, matrices, and air voids are clearly distinguishable in these images. The acquired image stacks were then used to develop the mesostructural models of AC, which will be discussed in the subsequent section.

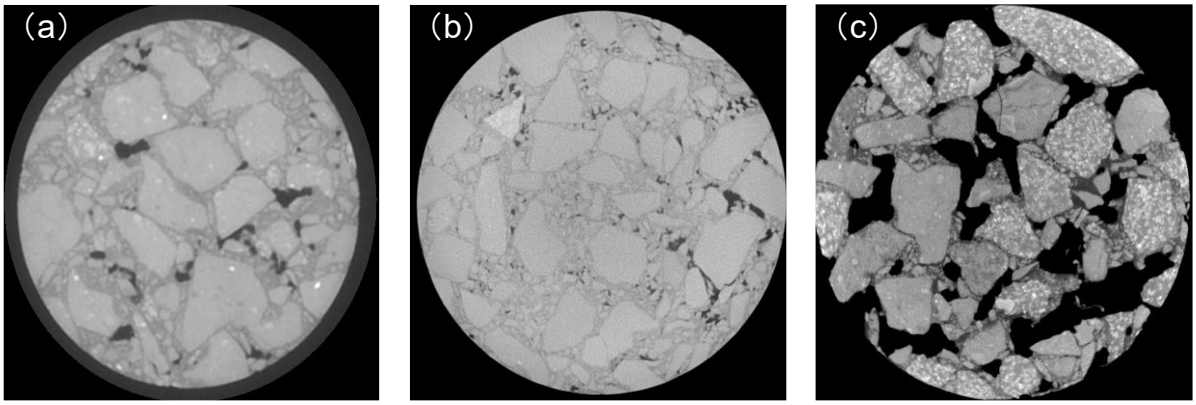

Figure 5 Scanned CT images of (a) SMA10; (b) AC20; and (c) PA13

4. Model development and computational study

4.1. Micromechanical modeling of CR

CR is a sandwich-like structure consisting of the ITZ, large filler particles (contact points), and asphalt mastic (Tan et al., 2023). To predict the viscoelastic properties of CR under T&C conditions, simplified microstructural models for CR were developed, as shown in Figure 6. These CR models are axisymmetric and have a total height (H) of 0.1 mm and a particle radius (R) of 0.04 mm. The L/R ratio is used as a parameter to represent contact point density, with higher values indicating lower densities. Previous research has shown that an L/R value of 2.5 provides reasonably accurate predictions for the viscoelastic properties of AC under T&C conditions (Tan et al., 2023). In contrast to the CR in compression, cohesive zone elements were inserted into the surface of the filler particle to simulate the separation between the ITZ and the particle. In the developed CR models, the measured viscoelastic properties shown in Figure 3 were applied to the matrix zone. The ITZ and particle were considered as elastic materials with elastic moduli of 40 GPa and 80 GPa, respectively. For the dynamic simulation, the bottom surface of the model was fixed, and a 10^{-4} compressive/tensile strain was applied on the top surface. The steady-state dynamic (SSD) method, known for its efficiency and accuracy in modeling the dynamic performance of asphalt materials (Cao et al., 2016; Leng et al., 2021; Tan et al., 2022), was employed to predict the tensile and compressive complex modulus master curves from 10^{-6} Hz to 10^{6} Hz. Figure 7 illustrates the predicted master curves of CR for SMA10 in T&C. It can be observed that the unique structure of AC's CR results in higher moduli in compression compared

to tension, with the difference decreasing at higher frequencies. The predicted master curves were converted to Prony series, which were then used as the material properties of CR in the micromechanical model of AC.

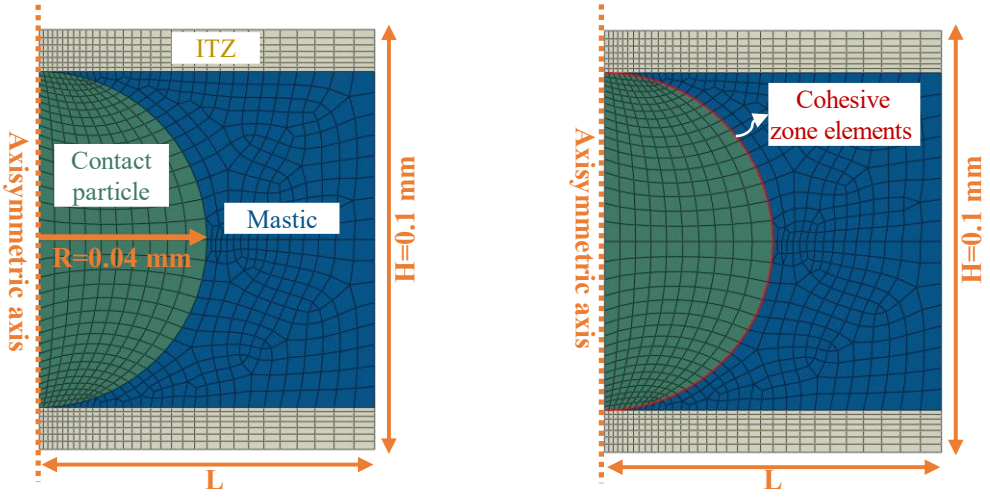

(a) In compression (b) In tension

Figure 6 CR models

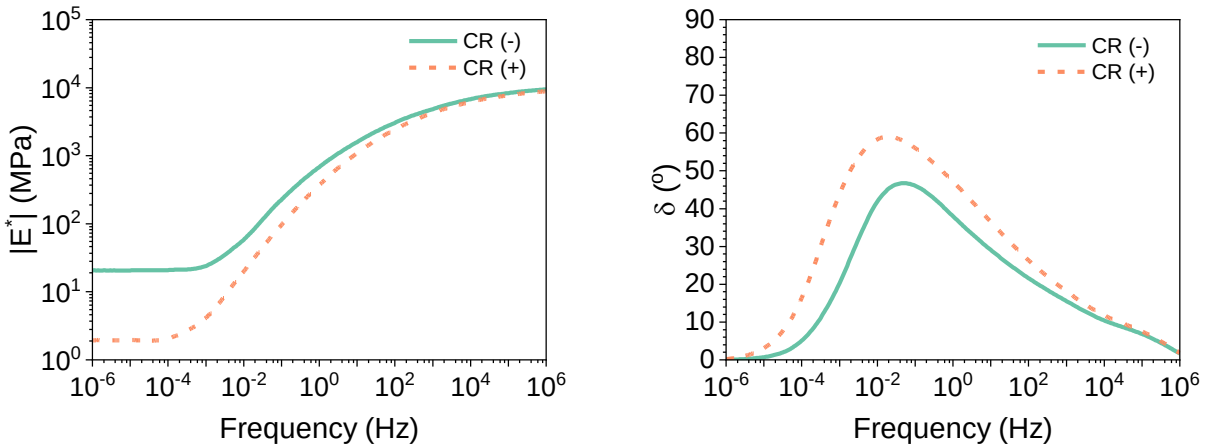

(a) Dynamic Modulus (b) Phase angle

Figure 7 Predicted master curves of SMA10's CR in T&C at 20 °C

4.2. Micromechanical modeling of AC

The modeling approach proposed in previous studies was adopted to generate the image-based models for the three AC mixtures, i.e., SMA10, AC20, and PA13 (Tan et al., 2023, 2022). As shown in Figure 8, through image segmentation, CR identification, and mesh generation, the microstructural models of AC mixtures can be developed. SDT, i.e., surface distance threshold, defining the surface distance between aggregates, is used to identify the CRs in mixtures. Based on the findings of (Tan et al., 2023,

2022), an SDT value of 0.1 mm is suitable to capture the CRs in the AC mixture. By applying meshing techniques, microstructural models consisting of four phases - aggregate, matrix (FAM), air void (empty zone), and CR - can be created. The volumetric proportions of the generated models and the real specimens for the three studied AC mixtures are listed in Table 1. It can be found that the generated models have very close volumetric compositions to the real AC mixtures. The CR only occupies a tiny volumetric fraction (lower than 3.2%) in the AC mixtures. Notably, the open-graded PA13 exhibits the highest CR volumetric proportion (approximately 3.2%), followed by SMA10 (approximately 1.5%), and AC20 with the lowest proportion (approximately 0.6%). This indicates that the degree of aggregate-to-aggregate interaction is strongest in PA13 among the considered mixtures.

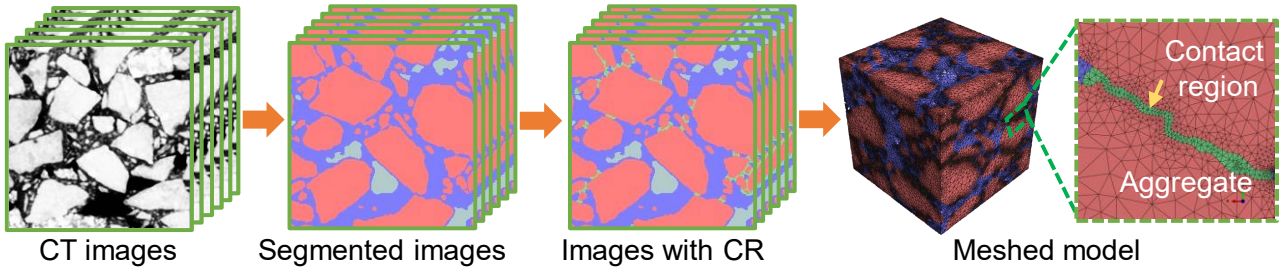

Figure 8 CT model generation (Tan et al., 2023)

Table 1 Volumetric properties of real AC mixtures and their corresponding models (%)

Sample ID	Aggregate	Matrix	Air void	Contact region (CR)
Real SMA10 specimen	63.5	31.6	4.5	-
SMA10 model	62.5	31.7	4.3	1.5
Real AC20 specimen	55.8	40.7	3.5	
AC20 model	54.5	41.6	3.2	0.6
Real PA13 specimen	65.6	16.4	18	
PA13 model	69.6	11.8	15.3	3.2

The AC models developed in this study considered aggregates as elastic materials with a Young's modulus of 80 GPa and Poisson's ratio of 0.2. The viscoelastic properties of the matrix (FAM) were determined using the Prony series based on the DSR measurement results (Figure 3). The material properties of CR in T&C were obtained from the developed CR model in Section 4.1. Depending on the loading mode of the AC model, either the predicted tensile or compressive viscoelastic properties (Figure 7) were assigned to the CR phase. Figure 9 illustrates the meshed models generated for the considered AC mixtures. Cubic samples with a length of 20 mm were developed for SMA10 and PA13, while a larger cubic model size of 30 mm was adopted for AC20 due to its larger aggregate size

compared to the other mixtures. Three replicates were generated for each mixture. The linear tetrahedral element (C3D4) was used for meshing the models. The average number of elements in the developed models for SMA10, AC20, and PA13 was 5.9 million, 4.5 million, and 7.4 million, respectively. It is important to note that the presence of thin matrix layers in PA13 resulted in a significant increase in the number of elements in the generated model. For dynamic modeling, the bottom face of the AC model was fixed, and a 10^{-4} compressive/tensile strain was applied to the top surface. Through the simulation, the dynamic response of AC in tension and compression within the frequency range of 10^{-6} Hz to 10^{6} Hz was predicted.

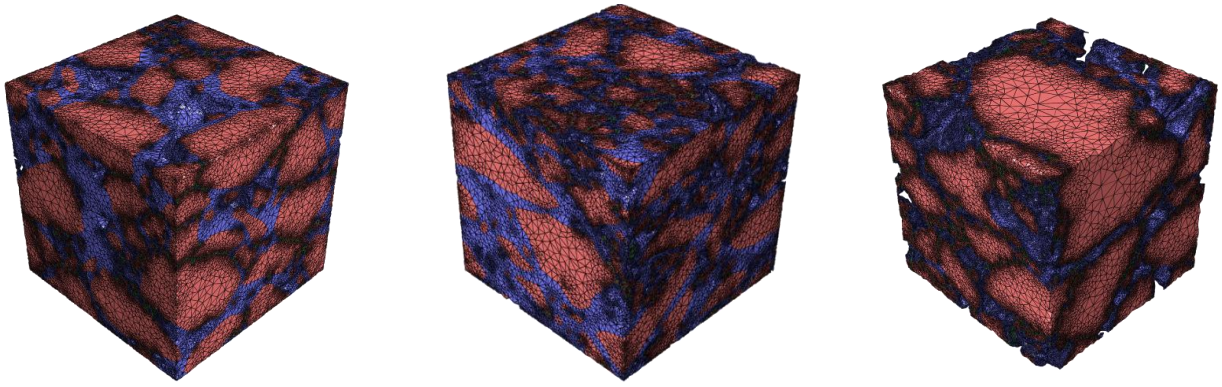

(a) SMA10 (b) AC20 (c) PA13

Figure 9 Meshed AC models of the three AC mixtures

5. Results and Discussion

In this section, the predicted master curves of considered AC mixtures in T&C will be first analyzed and compared to the corresponding master curve developed using experimental measurements. The principal stress distributions will then be discussed to illustrate the internal stress response of AC in T&C. In addition, the stress-strain response of AC in T&C in three different phases (i.e., aggregate, matrix, and CR) will also be analyzed statistically. In this context, probability distributions and average stress (strain) in all three phases were calculated and compared. For instance, in the aggregate phase, the absolute maximum principal stress (strain) and the corresponding volume of each aggregate element were extracted from ABAQUS to obtain the probability distribution. MATLAB codes were then used to sort the aggregate elements based on their absolute maximum principal stresses (strains) in ascending order. Eq. (6) and Eq. (7) represent the mathematical formulation for developing the probability distribution.

$$f(\sigma_i) = \frac{V_{\sigma_i}}{\sum V_{\sigma_i}} \quad (6)$$

$$g(\varepsilon_i) = \frac{V_{\varepsilon_i}}{\sum V_{\varepsilon_i}} \quad (7)$$

where $f(\sigma_i)$ and $g(\varepsilon_i)$ represent the density functions of stress and strain, respectively; σ_i and ε_i denote the ith absolute maximum principal stress and strain, while V_{σ_i} and V_{ε_i} represent their corresponding volume. Further, the volumetric average stress and strain can be calculated as follows:

$$\bar{\sigma}_V = \frac{\sum \sigma_i V_{\sigma_i}}{\sum V_{\sigma_i}} \quad (8)$$

$$\bar{\varepsilon}_V = \frac{\sum \varepsilon_i V_{\varepsilon_i}}{\sum V_{\varepsilon_i}} \quad (9)$$

where $\bar{\sigma}_V$ and $\bar{\varepsilon}_V$ are the volumetric average stress and strain, respectively.

5.1. Master curves of AC

Figure 10 presents the predicted master curve of AC mixtures in T&C. Although some differences exist, the predicted compressive and tensile master curves of the three AC mixtures still show good agreement with the experimental ones, indicating that the developed model can reasonably predict the mechanical performance of AC. These divergences could potentially be attributed to fluctuations in FAM measurements and variations within the CT model generation process. Similar to the measured master curves, the predicted master curves in tension also display much lower dynamic moduli but higher phase angles in the lower frequency range. Such an outcome is somewhat expectable due to the larger difference in stiffness between the matrix and aggregates at lower loading rates. It is also consistent with the findings of the previous studies (Cheng et al., 2021; Khanal and Mamlouk, 1995; Lytton et al., 2018). These results further confirm that aggregate contact is a critical factor contributing to the tension-compression asymmetry in AC. In terms of the degree of asymmetry, PA13 exhibits the highest degree of asymmetry, followed by SMA10 and AC20. For example, at a frequency of 10^{-4} Hz, the compressive modulus of PA13 is approximately twenty times higher than the tensile modulus, while the differences for SMA10 and AC20 are five and two times, respectively. Additionally, the peak tensile phase angles are 31%, 15%, and 43% higher than their corresponding values in compression mode for SMA10, AC20, and PA13, respectively. These findings are consistent with the volumetric percentages of CR (refer to Table 1), where PA13 has the highest volumetric percentage of CR.

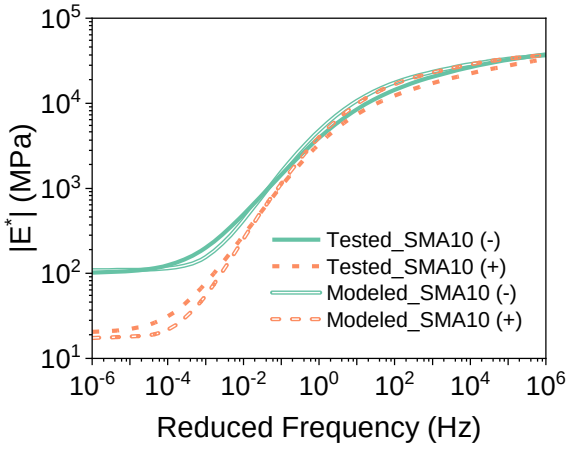

(a) Dynamic modulus of SMA10

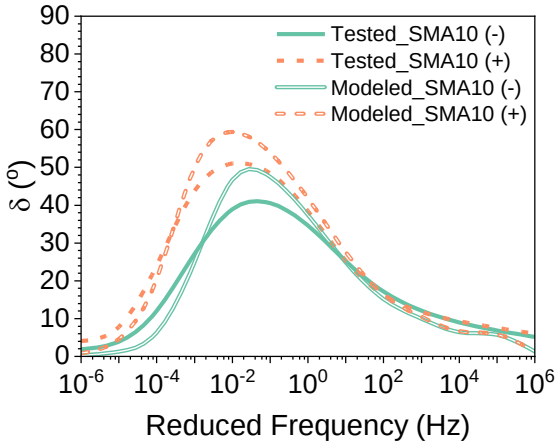

(b) Phase angle of SMA10

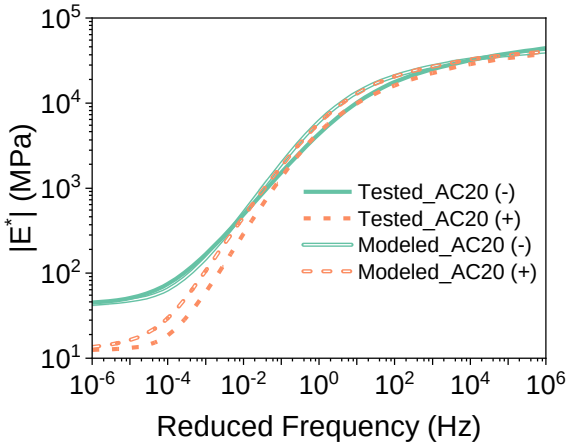

(c) Dynamic modulus of AC20

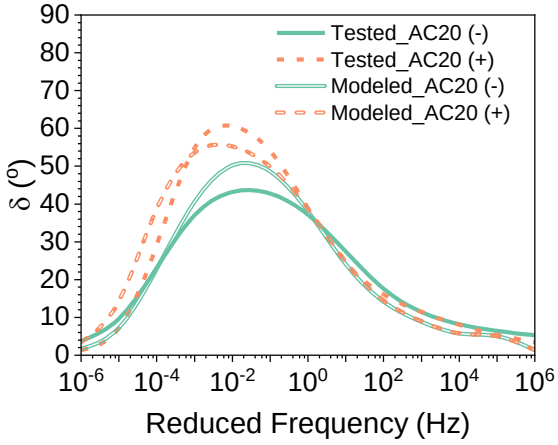

(d) Phase angle of AC20

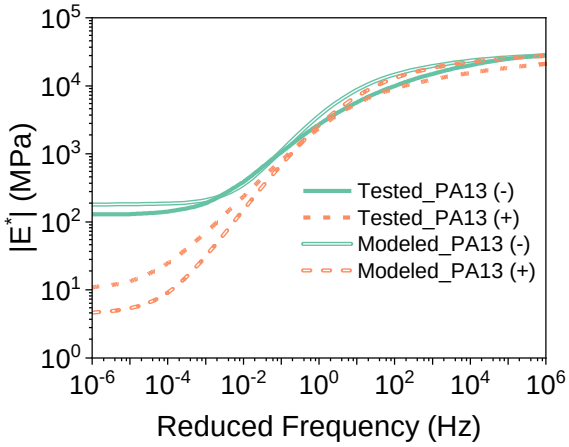

(e) Dynamic modulus of PA13

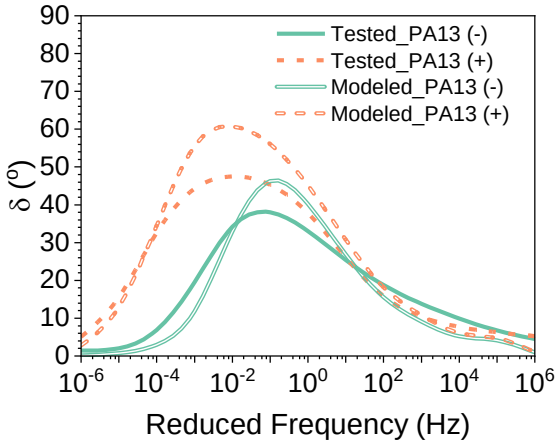

(f) Phase angle of PA13

Figure 10 Predicted and measured master curves of the three AC mixtures in T&C

5.2. Stress and strain analysis

Figure 11 presents the maximum principal stress distributions of AC in T&C. To provide a concise

representation, only the stress distributions of SMA10 are shown here, while those of AC20 and PA13 are included in the appendix. At a high frequency of 10^6 Hz (Figure 11 (b) and (d)), all three phases exhibit high stress levels regardless of the loading mode (tension or compression). This response can be attributed to the stiffening effect of the matrix phase (FAM). As the frequency increases, the weak matrix becomes stiffer, leading to improved stress transfer efficiency. However, this stiffening matrix also diminishes the influence of aggregate contacts. Consequently, the tension-compression asymmetry becomes less significant at higher frequencies, which explains the convergence of the master curves in tension and compression (Figure 10) with increasing loading frequency. On the other hand, at a low frequency of 10^{-6} Hz, stress is primarily concentrated in the aggregate phase (Figure 11 (a) and (c)). In compression (Figure 11 (c)), the aggregate and CR phases exhibit significantly higher stress compared to the AC mixtures under tension (Figure 11 (a)). This difference can be attributed to the effect of aggregate contact and its characteristics. In compression, the aggregates are pushed closer together, resulting in improved load transfer efficiency through stiff aggregate contacts (contact points) and higher stress in the aggregate and CR phases. However, in tension, the aggregates are pulled apart, rendering aggregate contacts ineffective. Consequently, the aggregate and CR phases in tension are expected to exhibit lower stress levels compared to compression.

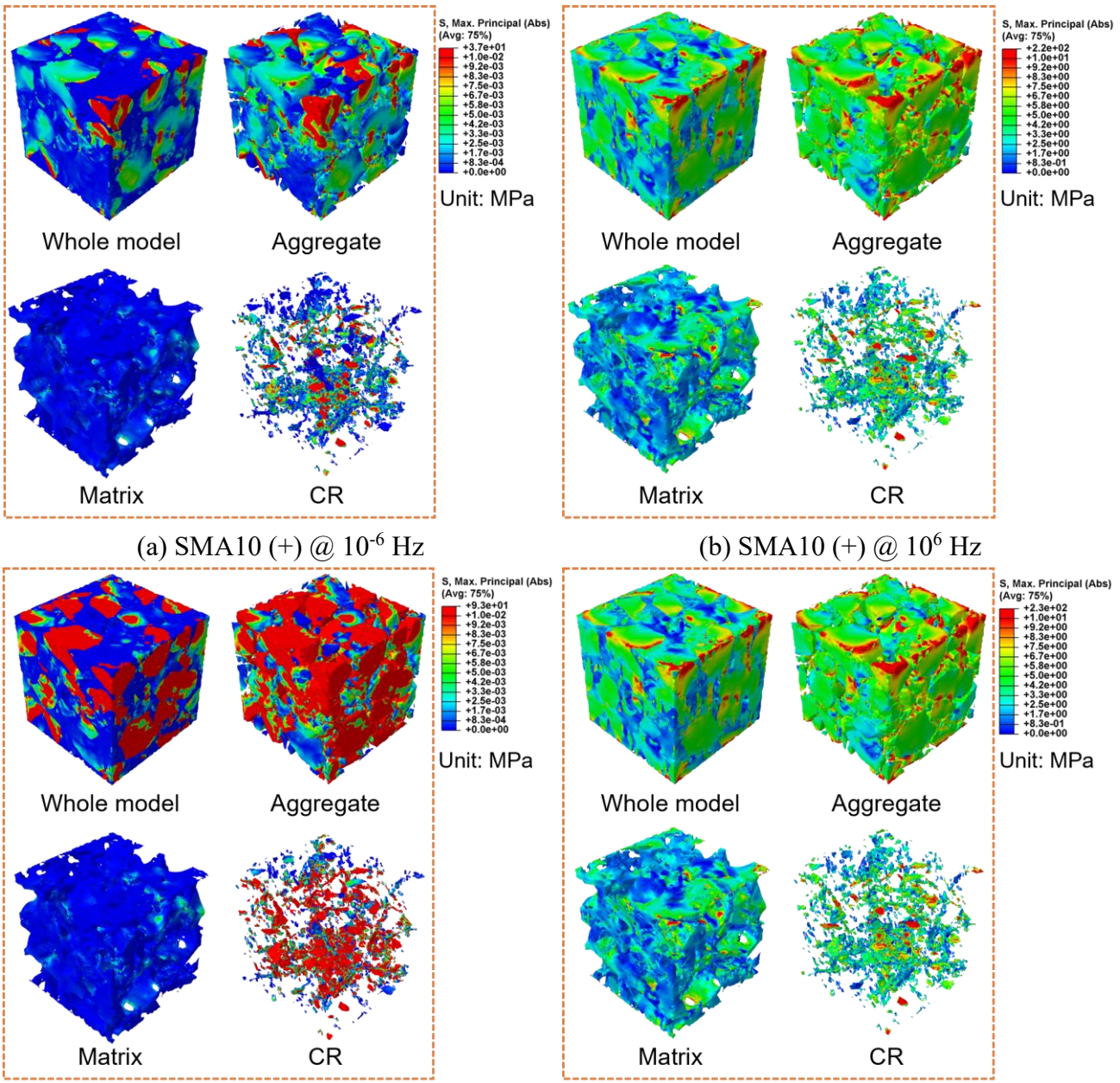

(a) SMA10 (+) @ 10^{-6} Hz (b) SMA10 (+) @ 10^{6} Hz

(c) SMA10 (-) @ 10^{-6} Hz (d) SMA10 (-) @ 10^{6} Hz

Figure 11 Maximum principal stress distributions of SMA10 in T&C

The stress probability distributions in the three phases - aggregate, matrix, and CR - were calculated using Eq. (6). Figure 12 depicts the probability distributions of the maximum principal stress for the three AC mixtures. It is evident that, unlike the stress distributions at 10^{-6} Hz, the stress probability distributions in tension (purple color) and compression (red color) almost overlap and converge to a narrow stress range at the high frequency of 10^{6} Hz. When comparing the stress probability distributions among the three phases, the aggregate phase (Figure 12(a), (d), and (g)) exhibits the highest stress concentration, displaying a narrow stress range. In contrast, the CR phase

(Figure 12(c), (f), and (i)) shows the lowest stress concentration. This difference can be attributed to the location-dependent stress distribution in the CR. The CR located between the aggregates in the load transfer chains experiences high stresses similar to the aggregate phase, while the CR situated outside the main load transfer path exhibits relatively lower stresses. Among the three AC mixtures, the aggregate phase of PA13 (Figure 12(g)) displays the narrowest stress range, followed by SMA10 (Figure 12(a)) and AC20 (Figure 12(d)), indicating the highest stress concentration in the aggregate phase of the open-graded AC mixture. Additionally, it is interesting to note that at lower loading frequencies, the stress distribution in the aggregate and CR phases in compression (blue color) is shifted to the right compared to tension (orange color), indicating higher stress ranges. However, the stress distributions in the matrix phase remain almost unchanged in both T&C. This suggests that the stiffness improvement in compression at lower frequencies is primarily contributed by the aggregate and CR phases rather than the matrix phase. Furthermore, the developed stress chain by the aggregate and CR phases significantly enhances stress transmission in AC.

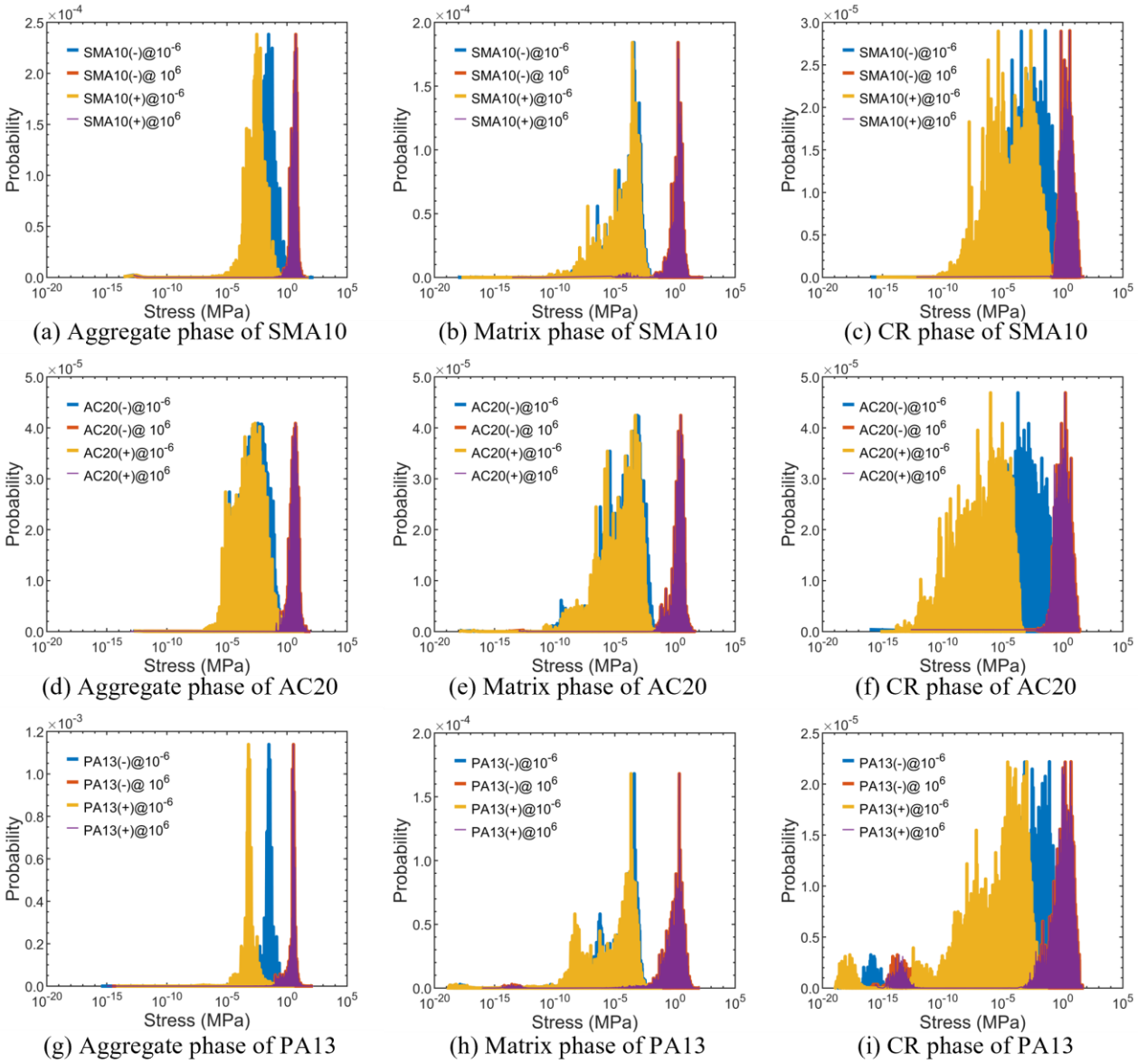

Figure 12 Probability distributions of maximum principal stress in different phases of the three AC mixtures

The strain probability distributions in all three phases of the AC mixtures were calculated using Eq. (7). Figure 13 displays the probability distributions of maximum principal strain. Similar to the stress probability distributions, higher frequencies result in a narrower strain range. Additionally, compared to the strains at low frequencies (blue and orange colors), the shift towards higher strain levels in the matrix and CR phases at high frequencies (red and purple colors) is relatively insignificant. However, the aggregate phase (Figure 13(a), (d), and (g)) exhibits a notable shift from low strain levels around 10^{-7} to high strain levels around 10^{-4}, indicating that the increase in frequency primarily affects

the strain in the aggregate phase. Furthermore, in comparison to tension (orange color), compression (blue color) leads to further increases in strain in the aggregate phase.

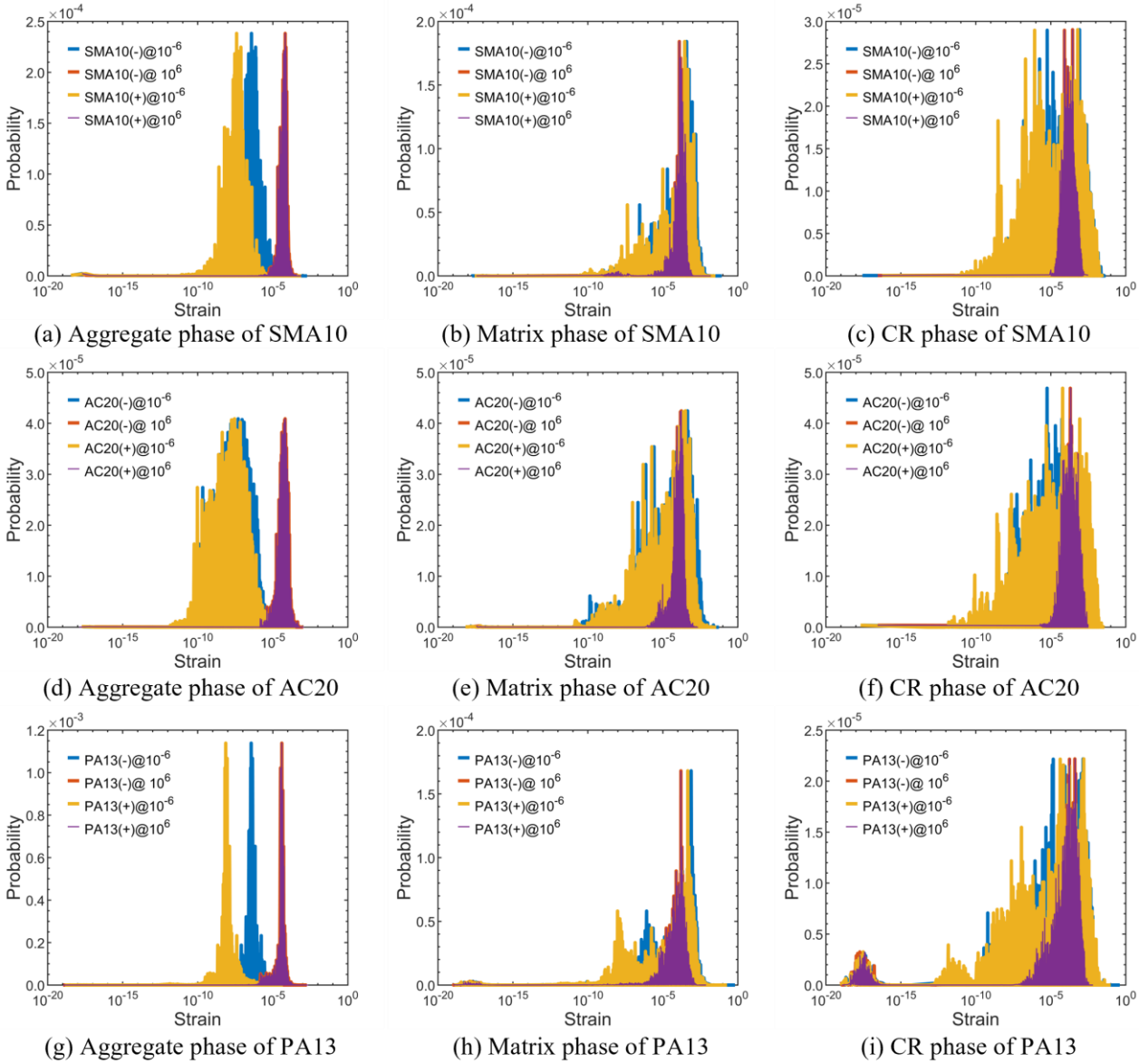

(a) Aggregate phase of SMA10 (b) Matrix phase of SMA10 (c) CR phase of SMA10

(d) Aggregate phase of AC20 (e) Matrix phase of AC20 (f) CR phase of AC20

(g) Aggregate phase of PA13 (h) Matrix phase of PA13 (i) CR phase of PA13

Figure 13 probability distribution of maximum strain in different phases of the three AC mixtures

The average stress in different phases was calculated using Eq. (8). Figure 14 displays the average stress in the various phases of the AC mixtures. At low frequencies (Figure 14(a) and (c)), the average stress in the matrix phase is significantly lower than the corresponding values in the aggregate and CR phases. However, at higher frequencies, the stress in the matrix phase increases and becomes comparable to the stress in the aggregate and CR phases due to the stiffening effect (Figure 14(b) and (d)). Additionally, based on Figure 14(a) and (c), it is evident that at lower frequencies, the average

stress in compression (Figure 14(a)) is much higher than the corresponding stress in tension (Figure 14(c)). Among the three AC mixtures, it is interesting to note that at 10^{-6} Hz (Figure 14(a) and (c)), the aggregate phase of PA13 exhibits the highest stress in compression and the lowest stress in tension. This response is closely related to the internal structure of the open-graded mixture. The increased aggregate contacts in PA13 facilitate better load transfer among aggregates, resulting in higher stress in compression. However, the higher air void content (18%) and lower FAM matrix content in PA13 have an adverse effect on stress transmission through the matrix phase, leading to lower stress in tension for the open-graded PA13.

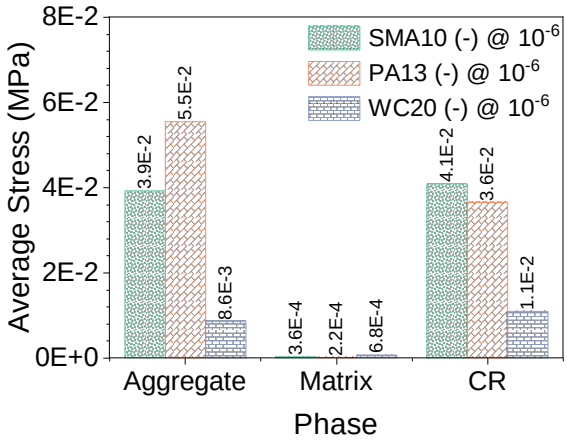

(a) In compression at 10^{-6} Hz

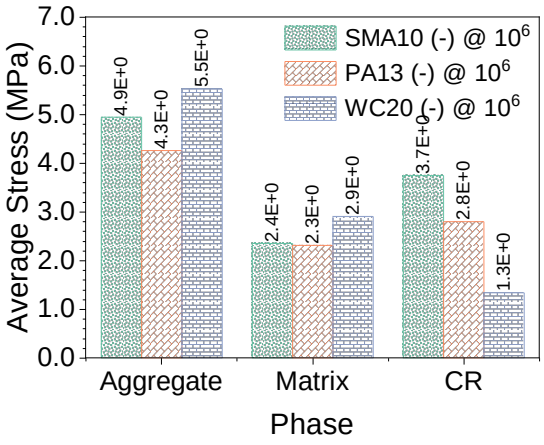

(b) In compression at 10^{6} Hz

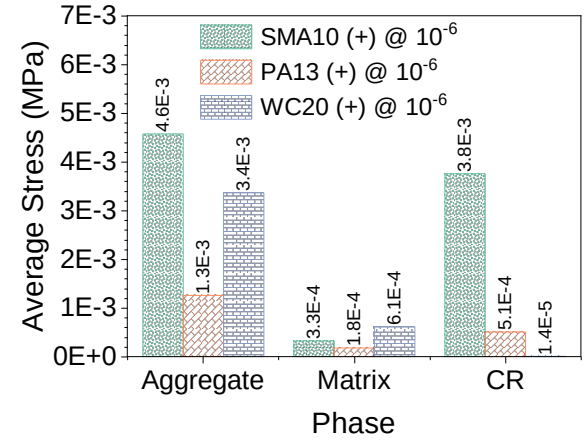

(c) In tension at 10^{-6} Hz

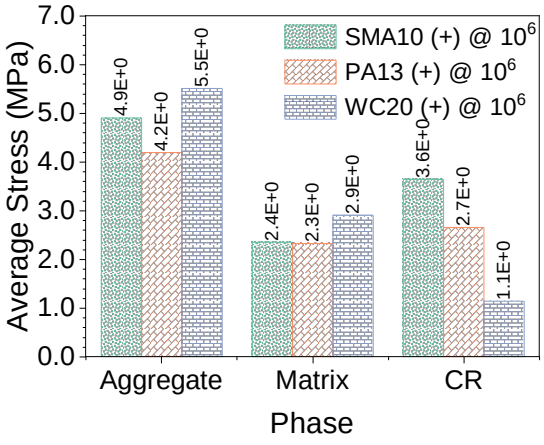

(d) In tension at 10^{6} Hz

Figure 14 Average stresses in AC's three phases: Aggregate, matrix, and CR

The average strain in the three phases of AC was calculated using Eq. (9). Figure 15 illustrates the average strain in different phases of the three AC mixtures. The plot clearly shows significantly higher average strains in the matrix and CR phases compared to the aggregate phase, regardless of the

loading mode and frequency. As the frequency increases, the strain in the aggregate phase also increases significantly, although it remains much lower than the corresponding values in the matrix and CR phases. It is worth noting that, unlike the case with average stress, the strain discrepancies are generally insignificant, except for the CR phase of AC20 under compression at 10^{-6} Hz. This exception can be attributed to the characteristics of the dense-graded AC20, where the stiffer matrix (FAM) and lower volumetric proportion of CR weaken the role of CR in stress transmission, resulting in lower strain in the CR phase for AC20 in compression.

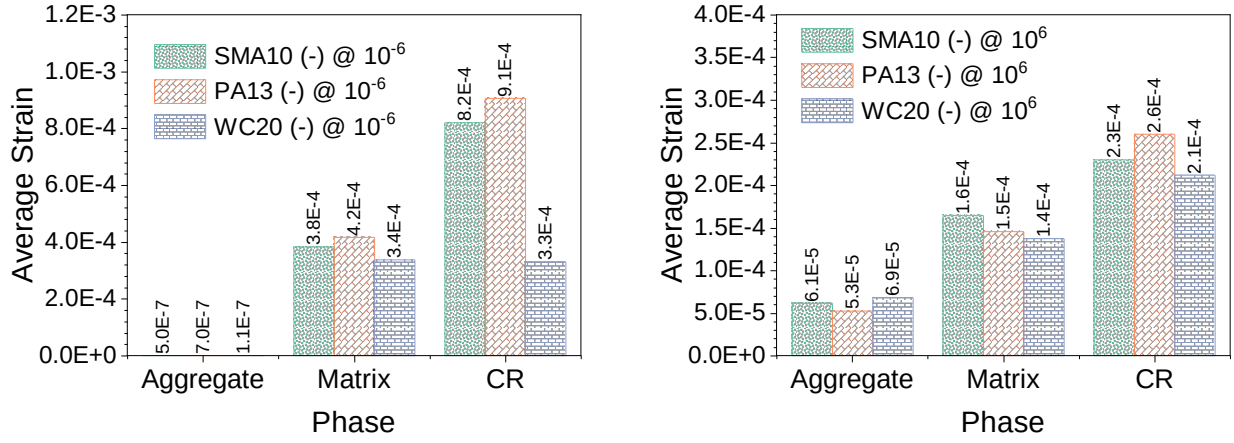

(a) In compression at 10^{-6} Hz (b) In compression at 10^{6} Hz

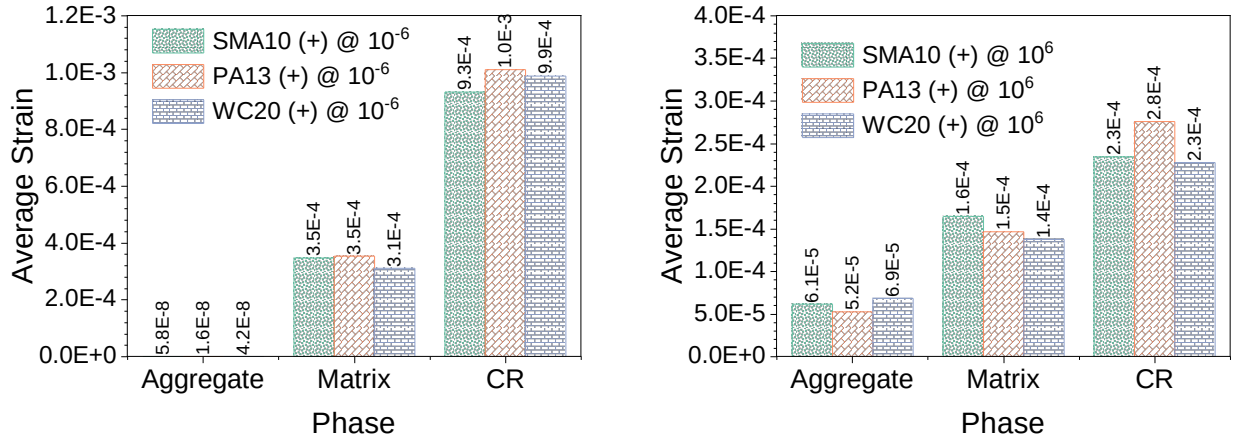

(c) In tension at 10^{-6} Hz (d) In tension at 10^{6} Hz

Figure 15 Average strains in AC's three phases: Aggregate, matrix, and CR

The relative ratios of stress and strain between different phases were calculated to assess the disparities between them. Figure 16 illustrates the average stress in the aggregate and CR phases relative to the average stress in the matrix phase. It is evident that under compression at 10^{-6} Hz, the stresses in the aggregate and CR phases are significantly higher compared to the stress in the matrix

phase (Figure 16(a)). For instance, the average stress in the aggregate phase of PA13 is more than 250 times higher than that in the matrix phase, followed by SMA10 and AC20. Similarly, Figure 16(c) shows the stress in tension under low frequency loading conditions. The stress differences are reduced significantly, but the stress in the aggregate phase is still five times higher than that in the matrix phase. At 10^6 Hz, the stress differences in the three phases decrease to around two times due to the stiffening effect of the matrix (FAM) phase, as shown in Figure 17(b) and (d).

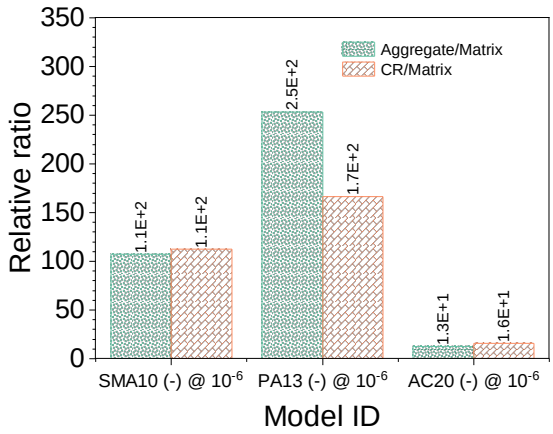

(a) In compression at 10^{-6} Hz

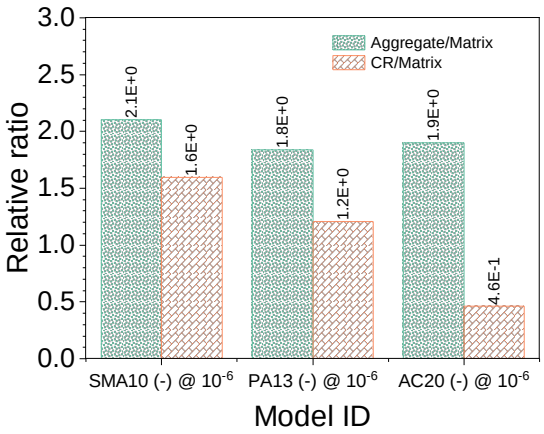

(b) In compression at 10^6 Hz

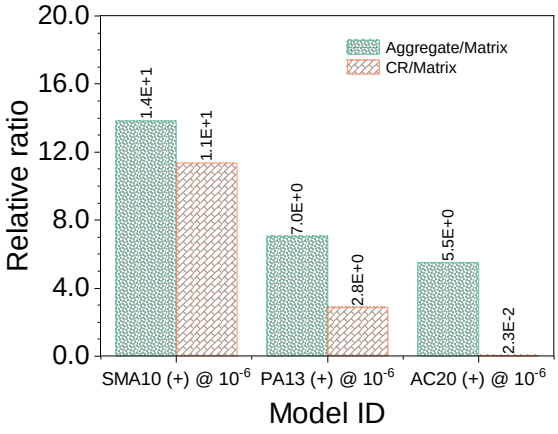

(c) In tension at 10^{-6} Hz

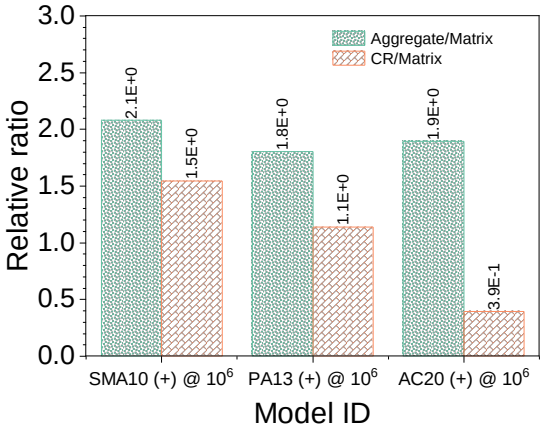

(d) In tension at 10^6 Hz

Figure 16 Relative stress ratios (Aggregate/Matrix and CR/Matrix)

Figure 17 depicts the average strain in the matrix phase relative to the average strain in the aggregate and CR phases. Similar to the stress, the strains in different phases exhibit significant variations at lower frequencies (Figure 17(a) and (c)). However, these differences narrow down to no more than three times at higher frequencies (Figure 17(b) and (d)). In compression at 10-6 Hz, Figure 17(a) shows that the strain in the matrix phase is more than 600 times higher than that in the aggregate

phase. These differences are further magnified in tension at 10-6 Hz (Figure 17(c)). The strain ratio between the matrix and aggregate phases exceeds 22,000 for PA13. These results indicate that deformation primarily occurs in the matrix phase at low frequencies, regardless of the loading mode, and the strain disparities among the three phases are more pronounced in tension than in compression for AC.

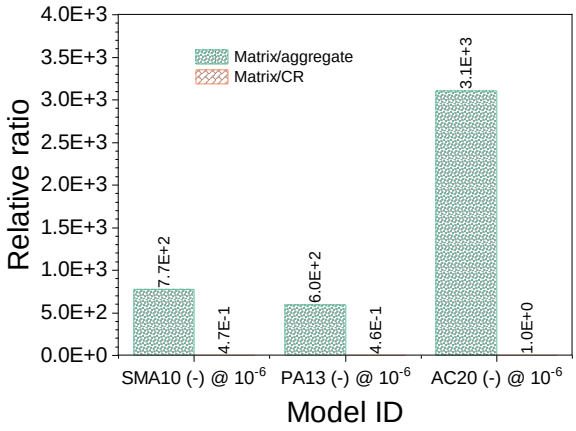

(a) In compression at 10^{-6} Hz

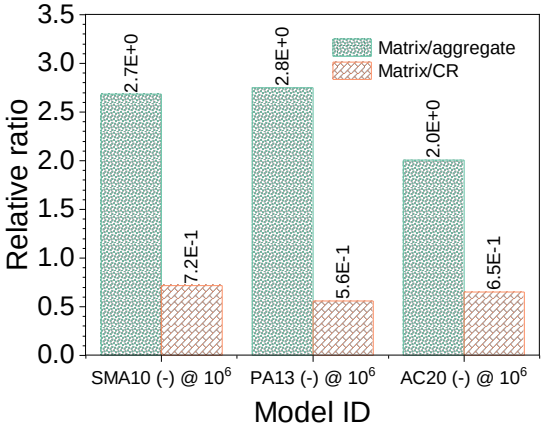

(b) In compression at 10^{6} Hz

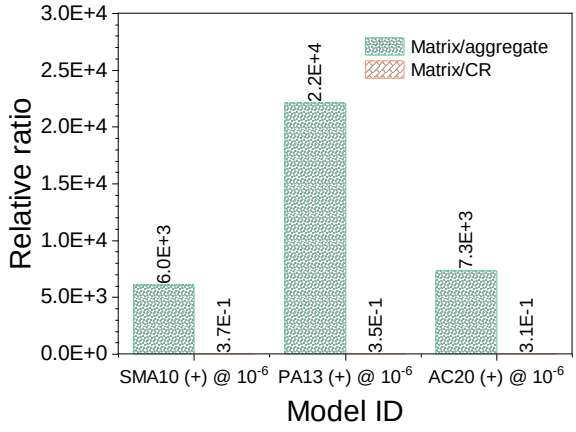

(c) In tension at 10^{-6} Hz

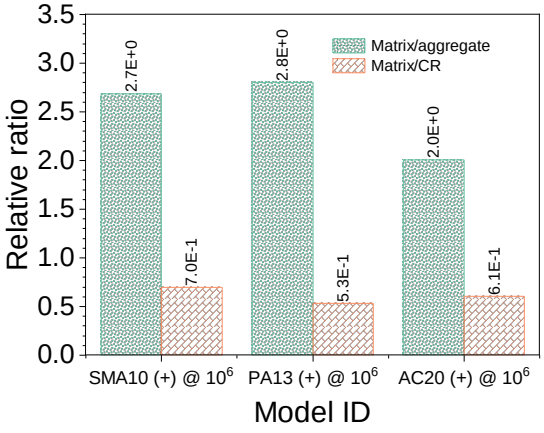

(d) In tension at 10^{6} Hz

Figure 18 Relative strain ratios (Matrix/aggregate and Matrix/CR)

6. Findings and Conclusions

This study developed image-based models of asphalt concrete (AC) that account for aggregate contacts. Dynamic simulations were conducted using the steady-state dynamics (SSD) method to characterize the global and local mechanical responses of three AC mixtures (gap-graded SMA10, dense-graded AC20, and open-graded PA13) in tension and compression (T&C). The main findings of this study are

as follows:

- The TC asymmetry of AC is primarily influenced by aggregate contacts. Incorporating contact regions (CR) into the micromechanical model of AC enables the quantification of the aggregate contact effect on AC's TC asymmetry.
- AC mixtures exhibit significant TC asymmetry at lower frequencies, with the open-graded mixture (PA13) displaying the highest asymmetry, followed by the gap-graded mixture (SMA10) and dense-graded mixture (AC20).
- In compression, the contact regions (CR) can bridge the large aggregates together, forming an interlocking structure that significantly improves stress transmission and compressive stiffness of AC.
- Regardless of the loading mode (tension/compression), as frequencies increase, stress in AC's three phases (aggregate, matrix, and CR) shifts towards higher stress domains, with the strain in the aggregate phase showing a particularly significant increase.
- At lower frequencies, stress mainly concentrates in AC's aggregate and CR phases, while strain primarily concentrates in the matrix phase.
- Stresses in different phases of AC exhibit significant variations, with more pronounced disparities at lower frequencies and for AC in compression compared to tension. At a low frequency of 10-6 Hz, the average stress in the aggregate phase of the open-graded PA13 was over 250 times higher than that in the matrix phase in compression, with similar observations in the dense-graded AC20. Although the differences reduced for tension, they still exceeded five times. These differences decrease with increasing frequencies and reach around two times at a high frequency of 106 Hz.
- Strains in different phases of AC also exhibit significant disparities, with more pronounced differences at lower frequencies and for AC in tension compared to compression. At a low frequency of 10^{-6} Hz, strains in the matrix phase were over 600 times higher than those in the aggregate phase in compression, with even larger differences in tension. With increasing frequencies, the differences decrease to no more than three times at a high frequency of 10^{6} Hz.

Considering the substantially lower tensile moduli of AC compared to its compressive moduli, it is

recommended to incorporate AC's tensile properties into pavement design. Additionally, techniques such as fiber reinforcement should be considered in mixture design to enhance the tensile resistance of AC layers.

References

AASHTO T 342, 2019. Standard method of test for determining dynamic modulus of hot mix asphalt (HMA).

Cai, X., Leng, Z., Kumar Ashish, P., Yang, J., Gong, M., 2023. Quantitative analysis of the role of temperature in the mesoscale damage process of semi flexible pavement composite through finite element method. Theor. Appl. Fract. Mech. 124, 103742. https://doi.org/10.1016/j.tafmec.2022.103742

Cai, X., Yang, J., Chen, X., Zhang, J., Zhang, H., 2020. Interlocking property evaluation of dual skeleton in semi-flexible pavement material by micromechanical model and X-ray computed tomography. Constr. Build. Mater. 254, 118934. https://doi.org/10.1016/j.conbuildmat.2020.118934

Cao, P., Jin, F., Zhou, C., Feng, D., 2017. Investigation on statistical characteristics of asphalt concrete dynamic moduli with random aggregate distribution model. Constr. Build. Mater. 148, 723–733. https://doi.org/10.1016/j.conbuildmat.2017.05.012

Cao, P., Jin, F., Zhou, C., Feng, D., Song, W., 2016. Steady-state dynamic method: An efficient and effective way to predict dynamic modulus of asphalt concrete. Constr. Build. Mater. 111, 54–62. https://doi.org/10.1016/j.conbuildmat.2016.02.071

Cao, P., Li, L., Yu, J., Zhang, Z., Jin, F., Zhao, Z., 2019. Research and application of random aggregate model in determining the fracture behavior of four-point bending beam with notch. Constr. Build. Mater. 202, 276–289. https://doi.org/10.1016/j.conbuildmat.2018.12.195

Cheng, H., Wang, Y., Liu, L., Sun, L., Zhang, Y., Yang, R., 2021. Estimating tensile and compressive moduli of asphalt mixture from indirect tensile and four-point bending tests. J. Mater. Civ. Eng. 33, 04020402. https://doi.org/10.1061/(ASCE)MT.1943-5533.0003476

Cho, K.S., 2016. Viscoelasticity of polymers, Springer Series in Materials Science. Springer Netherlands, Dordrecht. https://doi.org/10.1007/978-94-017-7564-9

Coenen, A.R., Kutay, M.E., Sefidmazgi, N.R., Bahia, H.U., 2012. Aggregate structure characterisation of asphalt mixtures using two-dimensional image analysis. Road Mater. Pavement Des. 13, 433–454. https://doi.org/10.1080/14680629.2012.711923

Dai, Z., Laheri, V., Zhu, X., Gilabert, F.A., 2021. Experimental study of compression-tension asymmetry in asphalt matrix under quasi-static and dynamic loads via an integrated DMA-based approach. Constr. Build. Mater. 283, 122725. https://doi.org/10.1016/j.conbuildmat.2021.122725

Du, C., Liu, P., Ganchev, K., Lu, G., Oeser, M., 2021. Influence of microstructure evolution of bitumen on its micromechanical property by finite element simulation. Constr. Build. Mater. 293, 123522. https://doi.org/10.1016/j.conbuildmat.2021.123522

Ferry, J.D., 1980. Viscoelastic properties of polymers, 3rd ed. John Wiley & Sons.

Gong, M., Chen, J., Sun, Y., 2023. Multiscale Finite-Element Analysis of Damage Behavior of Curved Ramp Bridge Deck Pavement Considering Tire–Bridge Interaction Effect. J. Eng. Mech. 149, 04023004. https://doi.org/10.1061/JENMDT.EMENG-6862

Hargett, E.R., Johnson, E.E., 1961. Strength properties of bituminous concrete tested in tension and compression, in: Highway Research Board Proceedings.

Jiang, J., Ni, F., Gao, L., Yao, L., 2017. Effect of the contact structure characteristics on rutting performance in asphalt mixtures using 2D imaging analysis. Constr. Build. Mater. 136, 426–435. https://doi.org/10.1016/j.conbuildmat.2016.12.210

Jiang, X., Gabrielson, J., Huang, B., Bai, Y., Polaczyk, P., Zhang, M., Hu, W., Xiao, R., 2022. Evaluation of inverted pavement by structural condition indicators from falling weight deflectometer. Constr. Build. Mater. 319, 125991. https://doi.org/10.1016/j.conbuildmat.2021.125991

Jiang, X., Zhang, M., Xiao, R., Polaczyk, P., Bai, Y., Huang, B., 2021. An investigation of structural responses of inverted pavements by numerical approaches considering nonlinear stress-dependent properties of unbound aggregate layer. Constr. Build. Mater. 303, 124505. https://doi.org/10.1016/j.conbuildmat.2021.124505

Jin, C., Wan, X., Liu, P., Yang, X., Oeser, M., 2021. Stability prediction for asphalt mixture based on evolutional characterization of aggregate skeleton. Comput.-Aided Civ. Infrastruct. Eng. 36, 1453–1466. https://doi.org/10.1111/mice.12742

Katicha, S.W., Flintsch, G.W., Loulizi, A., 2010. Bimodular analysis of hot-mix asphalt. Road Mater. Pavement Des. 11, 917–946. https://doi.org/10.1080/14680629.2010.9690313

Keshavarzi, B., Kim, Y.R., 2016. A viscoelastic-based model for predicting the strength of asphalt concrete in direct tension. Constr. Build. Mater. 122, 721–727. https://doi.org/10.1016/j.conbuildmat.2016.06.089

Khanal, P., Mamlouk, M., 1995. Tensile versus compressive moduli of asphalt concrete. Transp. Res. Rec. 144–150.

Kollmann, J., Lu, G., Liu, P., Xing, Q., Wang, D., Oeser, M., Leischner, S., 2019. Parameter optimisation of a 2D finite element model to investigate the microstructural fracture behaviour of asphalt mixtures. Theor. Appl. Fract. Mech. 103, 102319. https://doi.org/10.1016/j.tafmec.2019.102319

Kutay, M.E., Arambula, E., Gibson, N., Youtcheff, J., 2010. Three-dimensional image processing methods to identify and characterise aggregates in compacted asphalt mixtures. Int. J. Pavement Eng. 11, 511–528. https://doi.org/10.1080/10298431003749725

Lakes, R.S., 1998. Viscoelastic solids. CRC press.

Leng, Z., Tan, Z., Cao, P., Zhang, Y., 2021. An efficient model for predicting the dynamic performance of fine aggregate matrix. Comput. Civ. Infrastruct. Eng. 36, 1467–1479.

Levenberg, E., 2015. Viscoelastic tension-compression nonlinearity in asphalt concrete. J. Mater. Civ. Eng. 27, 04015048. https://doi.org/10.1061/(ASCE)MT.1943-5533.0001319

Li, P., Su, J., Ma, S., Dong, H., 2020. Effect of aggregate contact condition on skeleton stability in asphalt mixture. Int. J. Pavement Eng. 21, 196–202. https://doi.org/10.1080/10298436.2018.1450503

Ling, C., Arshadi, A., Bahia, H., 2017. Importance of binder modification type and aggregate structure on rutting resistance of asphalt mixtures using image-based multi-scale modelling. Road Mater. Pavement Des. 18, 785–799. https://doi.org/10.1080/14680629.2016.1189351

Ling, C., Bahia, H., 2018. Modelling of aggregates' contact mechanics to study roles of binders and aggregates in asphalt mixtures rutting. Road Mater. Pavement Des. 1–17. https://doi.org/10.1080/14680629.2018.1527716

Liu, P., Hu, J., Wang, D., Oeser, M., Alber, S., Ressel, W., Canon Falla, G., 2017. Modelling and evaluation of aggregate morphology on asphalt compression behavior. Constr. Build. Mater. 133, 196–208. https://doi.org/10.1016/j.conbuildmat.2016.12.041

Liu, P., Hu, J., Wang, H., Gustavo, F.C., Wang, D., Oeser, M., 2018. Influence of temperature on the mechanical response of asphalt mixtures using microstructural analysis and finite-element simulations. J. Mater. Civ. Eng. 30, 04018327. https://doi.org/10.1061/(ASCE)MT.1943-5533.0002531

Lu, G., Wang, C., Liu, P., Pyrek, S., Oeser, M., Leischner, S., 2019. Comparison of mechanical responses of asphalt mixtures under uniform and non-uniform loads using microscale finite element simulation. Materials 12, 3058. https://doi.org/10.3390/ma12193058

Lv, S., Liu, C., Yao, H., Zheng, J., 2018. Comparisons of synchronous measurement methods on various moduli of asphalt mixtures. Constr. Build. Mater. 158, 1035–1045. https://doi.org/10.1016/j.conbuildmat.2017.09.193

Lytton, R.L., Gu, F., Zhang, Y., Luo, X., 2018. Characteristics of undamaged asphalt mixtures in tension and compression. Int. J. Pavement Eng. 19, 192–204. https://doi.org/10.1080/10298436.2017.1279489

Lytton, R.L., Uzan, J., Fernando, E.G., Roque, R., Hiltunen, D., Stoffels, S.M., 1993. Development and validation of performance prediction models and specifications for asphalt binders and paving mixes (No. SHRP-A-357). Strategic Highway Research Program, Washington, DC, United States.

Monismith, C.L., Secor, K.E., 1962. Viscoelastic behavior of asphalt concrete pavements. Presented at the International Conference on the Structural Design of Asphalt Pavements, Ann Arbor, Michigan, pp. 728–760.

Nguyen, Q.T., Di Benedetto, H., Sauzéat, C., Nguyen, M.L., Hoang, T.T.N., 2016. 3D complex modulus tests on bituminous mixture with sinusoidal loadings in tension and/or compression. Mater. Struct. 50, 98. https://doi.org/10.1617/s11527-016-0970-x

Onifade, I., Jelagin, D., Birgisson, B., Kringos, N., 2016. Towards asphalt mixture morphology evaluation with the virtual specimen approach. Road Mater. Pavement Des. 17, 579–599. https://doi.org/10.1080/14680629.2015.1098561

Pister, K.S., Westmann, R.A., 1962. Analysis of viscoelastic pavements subjected to moving loads, in: International Conference on the Structural Design of Asphalt Pavements. Ann Arbor, Michigan.

Song, W., Deng, Z., Wu, H., Xu, Z., 2023. Cohesive zone modeling of I–II mixed mode fracture behaviors of hot mix asphalt based on the semi-circular bending test. Theor. Appl. Fract. Mech. 124, 103781. https://doi.org/10.1016/j.tafmec.2023.103781

Song, W., Xu, F., Wu, H., Xu, Z., 2021. Investigating the skeleton behaviors of open-graded friction course using discrete element method. Powder Technol. 385, 528–536. https://doi.org/10.1016/j.powtec.2021.03.012

Sun, Y., Zhang, Z., Gong, H., Zhou, C., Chen, J., Huang, B., 2022. 3D multiscale modeling of asphalt pavement responses under coupled temperature–stress fields. J. Eng. Mech. 148, 04022010. https://doi.org/10.1061/(ASCE)EM.1943-7889.0002089

Sun, Y., Zhang, Z., Wei, X., Du, C., Gong, M., Chen, J., Gong, H., 2021. Mesomechanical prediction of viscoelastic behavior of asphalt concrete considering effect of aggregate shape. Constr. Build. Mater. 274, 122096. https://doi.org/10.1016/j.conbuildmat.2020.122096

Tan, Z., Leng, Z., Jiang, J., Cao, P., Jelagin, D., Li, G., Sreeram, A., 2022. Numerical study of the aggregate contact effect on the complex modulus of asphalt concrete. Mater. Des. 213, 110342. https://doi.org/10.1016/j.matdes.2021.110342

Tan, Z., Yang, B., Leng, Z., Jelagin, D., Cao, P., Li, R., Zou, F., 2023. Multiscale characterization and modeling of aggregate contact effects on asphalt concrete's tension–compression asymmetry. Mater. Des. 232, 112092. https://doi.org/10.1016/j.matdes.2023.112092

Tschoegl, N.W., 1989. The phenomenological theory of linear viscoelastic behavior. Springer Berlin Heidelberg,

Berlin, Heidelberg. https://doi.org/10.1007/978-3-642-73602-5
Wollny, I., Hartung, F., Kaliske, M., Liu, P., Oeser, M., Wang, D., Canon Falla, G., Leischner, S., Wellner, F., 2020. Coupling of microstructural and macrostructural computational approaches for asphalt pavements under rolling tire load. Comput.-Aided Civ. Infrastruct. Eng. 35, 1178–1193. https://doi.org/10.1111/mice.12535
Zhang, Y., Leng, Z., 2017. Quantification of bituminous mortar ageing and its application in ravelling evaluation of porous asphalt wearing courses. Mater. Des. 119, 1–11. https://doi.org/10.1016/j.matdes.2017.01.052
Zhang, Y., Luo, R., Lytton, R.L., 2012. Anisotropic viscoelastic properties of undamaged asphalt mixtures. J. Transp. Eng. 138, 75–89. https://doi.org/10.1061/(ASCE)TE.1943-5436.0000302

APPENDIX

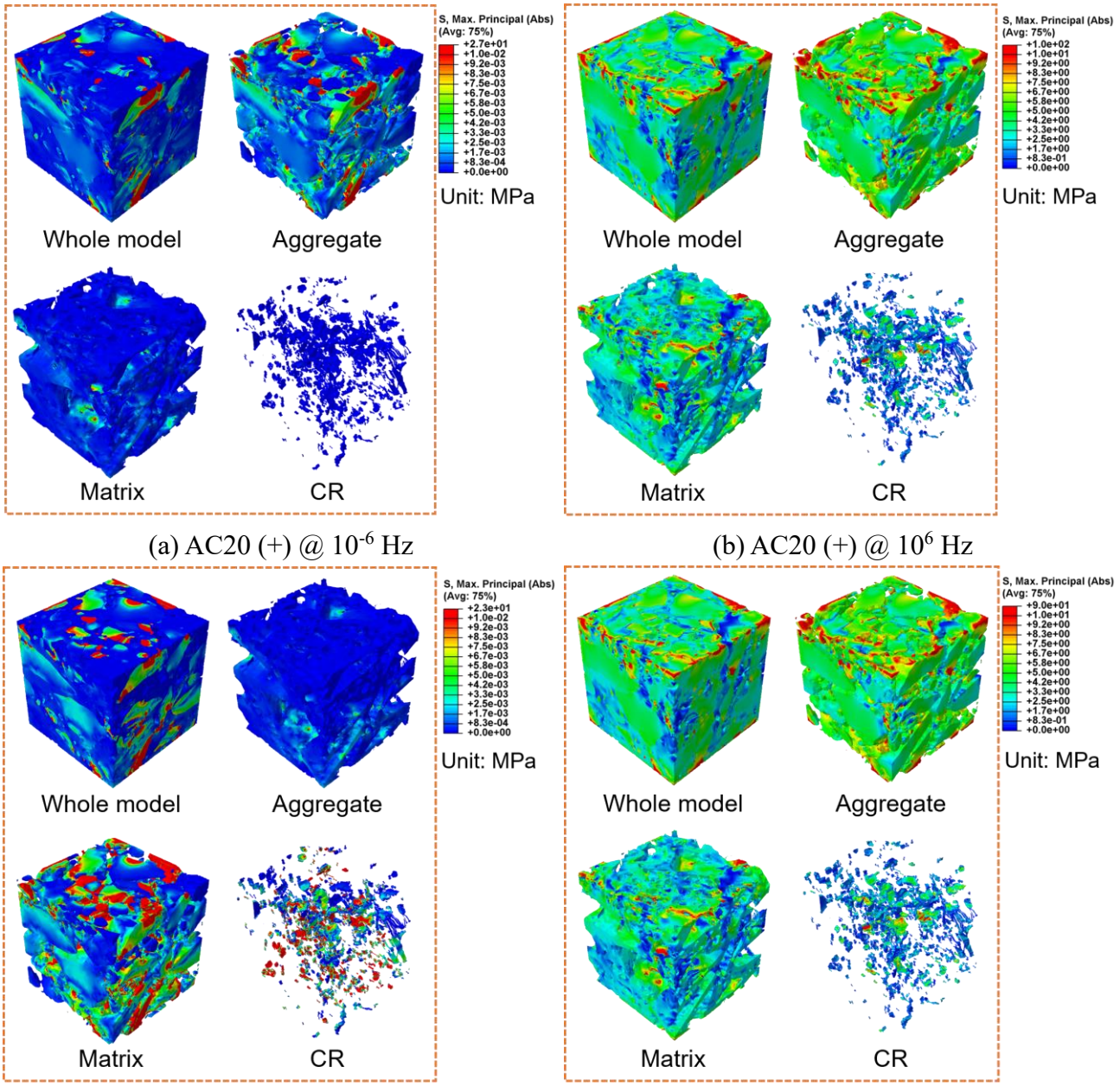

(a) AC20 (+) @ 10^{-6} Hz (b) AC20 (+) @ 10^{6} Hz

(c) AC20 (-) @ 10^{-6} Hz (d) AC20 (-) @ 10^{6} Hz

Figure A1 Maximum principal stress distributions of AC20

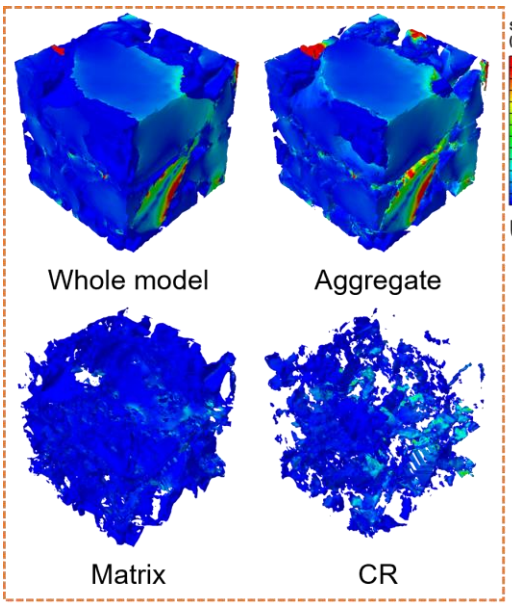

(a) PA13 (+) @ 10^{-6} Hz

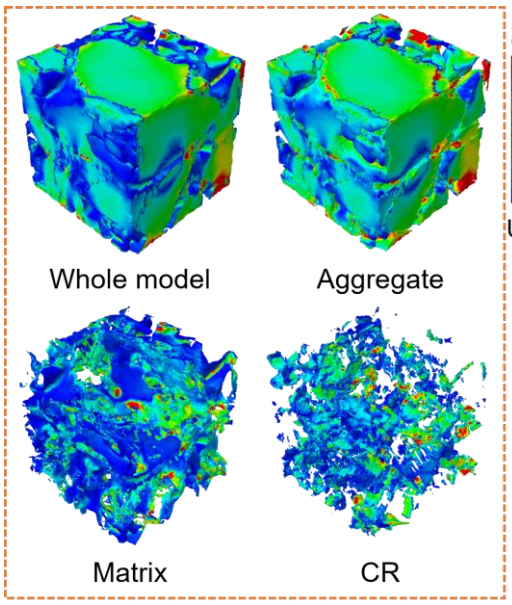

(b) PA13 (+) @ 10^{6} Hz

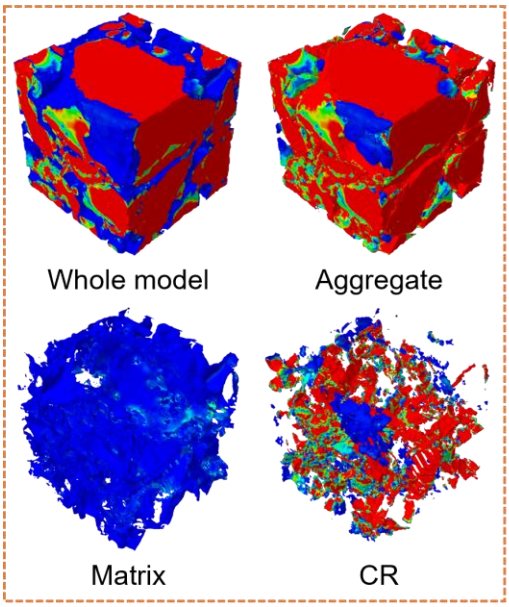

(c) PA13 (-) @ 10^{-6} Hz

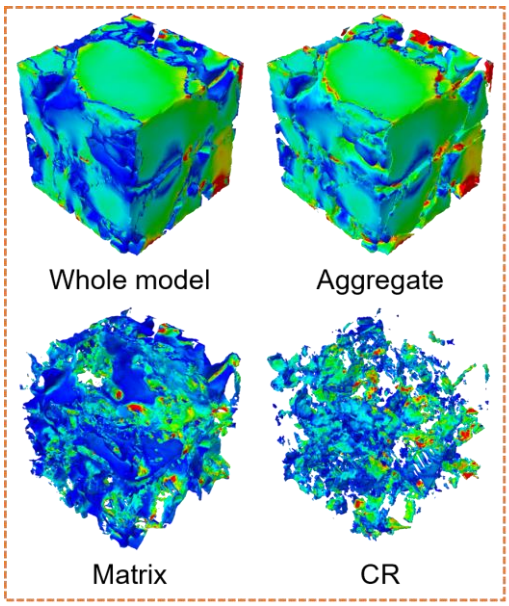

(d) PA13 (-) @ 10^{6} Hz

Figure A2 Maximum principal stress distributions of PA13

1